Volume 165, issues 17–18, September 2010 ISSN 0377-0257

ELSEVIER

Journal of Non-Newtonian Fluid Mechanics

Special Issue:
5th International Workshop on Non-Equilibrium Thermodynamics
Guest Editors: L.S. García-Colín, M. López de Haro and F. Vázquez

On-line Access via:
www.elsevier.com/locate/jnnfm

J. Non-Newtonian Fluid Mech. 165 (2010) 992–1004

Contents lists available at ScienceDirect

Journal of Non-Newtonian Fluid Mechanics

journal homepage: www.elsevier.com/locate/jnnfm

Atomistic simulation of crystallization of a polyethylene melt in steady uniaxial extension

Chunggi Baig [a,*], Brian J. Edwards [b,**]

[a] Department of Chemical Engineering, University of Patras & FORTH-ICE/HT, Patras, GR 26504, Greece
[b] Department of Chemical and Biomolecular Engineering, University of Tennessee, Knoxville, TN 37996, USA

ARTICLE INFO

Article history:
Received 17 November 2009
Received in revised form 15 April 2010
Accepted 16 April 2010

Keywords:
Flow-induced crystallization
Nonequilibrium Monte Carlo
Uniaxial elongational flow
Configurational temperature
Structure factor
Nonequilibrium free energy

ABSTRACT

We present simulation results of flow-induced crystallization of a dense polymeric liquid subjected to a strong uniaxial elongational flow using a rigorous nonequilibrium Monte Carlo method. A distinct transition between the liquid and the crystalline phases occurred at critical values of flow strength, with an abrupt, discontinuous transition of the overall chain conformation. The flow-induced crystalline phase matched quantitatively the experimental X-ray diffraction data of the real crystals remarkably well, including the sharp Bragg peaks at small wavenumbers, $k < 1.5\,\text{Å}^{-1}$, indicating the existence of a global long-range ordering. We also found that the enthalpy change ($\Delta H = 225$ J/g) during the phase transition was quantitatively very similar to the experimental heat of fusion (276 J/g) of polyethylene crystals under quiescent conditions. Furthermore, a detailed analysis of the configuration-based temperature provided a sound microscopic physical origin for the effective enhancement of the crystallization (or melting) temperature that has been observed in experiments. Simulation results also allow for the deduction of potential nonequilibrium expressions for thermodynamic quantities, such as temperature and heat capacity.

1. Introduction

In contrast to simple fluids such as water, polymers are highly complex macromolecules possessing a complicated internal microstructure characterized by a multiplicity of time and length scales. Fundamental knowledge of the mutual interplay between microscopic molecular structure and macroscopic observables is of critical importance to understanding various thermodynamic and rheological phenomena [1,2]. As an example, the mechanical and optical properties of semi-crystalline fibrous materials are significantly enhanced relative to amorphous polymers, leading to a multi-billion dollar per year industry with a wide range of applications, such as clothing, fabrics, textiles, surgical instruments, military equipment, optical components, sensing devices, etc. Despite such practical importance and numerous directed research efforts in this field, the fundamental molecular mechanisms regarding how polymer molecules are oriented, aligned, and often crystallized from the liquid state under an external field are still not well understood yet. Such microscopic information would be practically very beneficial not only in tuning currently available materials to specific applications, but also in the development of novel polymeric materials via modifying chemical properties and molecular architectures.

Since the direct experimental observations in 1960s of flow-induced crystalline (FIC) phases occurring in many polymeric materials under certain conditions [3,4], numerous theoretical and experimental research efforts [5–20] have been directed over the past several decades to understand the crystallization process and the resulting structure. It is generally known that the kinetics of nucleation and crystal-growth, the FIC morphology, and its stability, are extremely sensitive to experimental conditions (e.g. temperature, pressure, molecular weight distribution, flow type, imposed strain and/or strain rate, etc.) in a very complicated fashion, which has often caused substantial confusion among researchers in the past (and still today) in their physical interpretations of FIC phenomena.

Despite numerous theoretical efforts to model flow-induced crystallization and experimental research to expose the basic process, many of the fundamental molecular mechanisms involving the crystallization kinetics and morphological development remain to be explored; for example, there is still a lack of capability of existing theories or experiments for elucidating how and why stresses generated under flow raise the melting or crystallization temperature of a polymeric material by orienting and deforming the constituent macromolecules at constant temperature [2,15,16,20].

In this respect, molecular simulation based upon first-principles is considered an important tool for the fundamental study of the

---

* Corresponding author. Tel.: +30 2610 965219; fax: +30 2610 965223.
** Corresponding author. Tel.: +1 865 974 9596; fax: +1 865 974 7076.
E-mail addresses: cbaig@iceht.forth.gr (C. Baig), bje@utk.edu (B.J. Edwards).

0377-0257/$ – see front matter © 2010 Elsevier B.V. All rights reserved.
doi:10.1016/j.jnnfm.2010.04.007

crystallization process, especially at atomistic time and length scales that are well below currently available experimental limits. Indeed, there have been several simulation studies in the past using molecular dynamics (MD) [21–23] and Monte Carlo (MC) [24,25] simulations. Although these works [21–25] provided valuable fundamental information on the kinetics of nucleation and morphological developments at molecular length scales, certain synthetic procedures for inducing the crystallization, rather than applying a rigorous Hamiltonian-based nonequilibrium flow algorithm [26], make direct connections between simulation and experiment difficult to interpret.

More recently, a direct nonequilibrium molecular dynamics (NEMD) study using an *n*-eicosane ($C_{20}H_{42}$) melt was performed under planar extensional flow [27], which demonstrated that the local intramolecular structure of the melt in a strong planar extension was quantitatively similar to that of the real crystal, experimentally obtained via x-ray diffraction. However, there was no detectable sign of global long-range ordering existing in the real crystal. Possible reasons for the absence of such large-scale ordering are (a) retardation of the long-range order due to the planar nature of the applied flow field (i.e., the neutrality of the third orthogonal direction, as opposed to the stretching and compression directions, allowed the molecular packing additional large degree of freedom that would not be present in a uniaxial flow with two compression directions), (b) thermostat artifacts that may occur in NEMD simulations at very high strain rates, and (c) the temperature used in those simulations (315 K) [27] was above the quiescent melting point of the real crystal (approximately 310 K). These problems are overcome in this work by adopting a nonequilibrium Monte Carlo methodology at multiple values of temperature that can (a) generate uniaxial elongational flow (which is currently not possible with NEMD due to the absence of the requisite periodic boundary conditions) and (b) intrinsically avoid possible thermostat artifacts.

Some preliminary results of this study have been presented in Ref. [28]. In this paper we present a detailed, comprehensive analysis of all the results to date.

2. Simulation methodology and systems studied

The nonequilibrium Monte Carlo (NEMC) simulations were performed using the methodology of Refs. [29–31]. This methodology has proven to be capable of generating realistic steady-state structures of flowing polymeric systems at various length scales [29,30]. The fundamental equation of thermodynamics for the internal energy of polymeric systems under flow is written as [1,32,33]

$$dU = TdS - PdV + \mu dN_{ch} + k_B T\boldsymbol{\alpha} : d(N_{ch}\tilde{\mathbf{c}}), \qquad (1)$$

where T denotes the temperature, S the entropy, P the pressure, V the system volume, μ the chemical potential, N_{ch} the number of chains, k_B Boltzmann's constant, and $\boldsymbol{\alpha}$ is the thermodynamic flow field tensor, which is conjugate to the dimensionless second-rank conformation tensor, $\tilde{\mathbf{c}} = 3\left\langle \boldsymbol{RR}\right\rangle / \left\langle R^2 \right\rangle_{eq}$. In the definition of the $\tilde{\mathbf{c}}$, $\mathbf{R}$ is the chain end-to-end vector and the angular brackets denote the ensemble average.

The coupling of the field $\boldsymbol{\alpha}$ with the conformation tensor $\tilde{\mathbf{c}}$ in the thermodynamic functions effectively drives the system away from the initial equilibrium states; e.g., based on the following probability density function in an expanded semi-grand statistical ensemble, $\{N_{ch}nPT\boldsymbol{\mu}^*\boldsymbol{\alpha}\}$,

$$\rho^{N_{ch}nPT\boldsymbol{\mu}^*\boldsymbol{\alpha}}(\mathbf{r}_1, \mathbf{r}_2, \ldots, \mathbf{r}_n, V) \sim \exp[-\beta(U^p(\mathbf{r}_1, \mathbf{r}_2, \ldots, \mathbf{r}_n, V) + PV - \sum_{k=1}^{n}\mu_k^* N_k - k_B T\boldsymbol{\alpha} : \sum_{k=1}^{N_{ch}}\tilde{\mathbf{c}}_k)]. \qquad (2)$$

Here $\beta \equiv 1/k_BT$, N_k is the number of chains of length k-mers, $n(= N_{ch} \times N)$ the total number of atoms in the system with the average number of atoms per chain, N. The $\{\mathbf{r}\} = \{\mathbf{r}_1, \mathbf{r}_2, \ldots, \mathbf{r}_n\}$ represent the space of the atomistic position vectors, U^p the potential energy of the system, and μ_k^* the relative chemical potential of the chain of length k-mers and $\tilde{\mathbf{c}}_k$ its conformation tensor. Eq. (2) implies that the system configurations are sampled according to the following modified Metropolis acceptance criterion,

$$p_{acc}^{N_{ch}nPT\boldsymbol{\mu}^*\boldsymbol{\alpha}} \sim \exp[-\beta(\Delta U^p + P\Delta V - \sum_{k=1}^{n}\Delta(\mu_k^* N_k) - k_B T\boldsymbol{\alpha} : \sum_{k=1}^{N_{ch}}\Delta\tilde{\mathbf{c}}_k)]. \qquad (3)$$

In order to impose a uniaxial elongational flow field, the form of $\boldsymbol{\alpha}$ used in this study was

$$\alpha = \begin{pmatrix} \alpha_{xx} & 0 & 0 \\ 0 & \alpha_{yy} & 0 \\ 0 & 0 & \alpha_{zz} \end{pmatrix}, \qquad (4)$$

where $\alpha_{yy} = \alpha_{zz} = -\alpha_{xx}/2$, as assuming the one-to-one correspondence between $\boldsymbol{\alpha}$ and the real velocity gradient tensor for uniaxial elongational flow [29].

All of the other thermodynamic functions can be derived from the above expressions through appropriate Legendre transformations. For instance, the extended Helmholtz free energy, A, and Gibbs free energy, G, of the nonequilibrium system are derived as

$$dA(T, V, N_{ch}, N_{ch}\tilde{\mathbf{c}}) = -SdT - PdV + \mu dN_{ch} + k_BT\boldsymbol{\alpha}{:}d(N_{ch}\tilde{\mathbf{c}}), \qquad (5)$$

and

$$dG(T, P, N_{ch}, \boldsymbol{\alpha}) = -SdT + VdP + \mu dN_{ch} - N_{ch}\tilde{\mathbf{c}} : d(k_BT\boldsymbol{\alpha}), \qquad (6)$$

respectively. A further definition of an intermediate free energy function is expressed as

$$A' = A - N_{ch}k_BT\boldsymbol{\alpha} : \tilde{\mathbf{c}} \qquad (7a)$$

such that

$$dA'(T, V, N_{ch}, \boldsymbol{\alpha}) = -SdT - PdV + \mu dN_{ch} - N_{ch}\tilde{\mathbf{c}} : d(k_BT\boldsymbol{\alpha}). \qquad (7b)$$

For more details of the fundamental aspects underlying the NEMC methodology, the reader may refer to Refs. [29–31].

In the present work, the NEMC simulations were carried out in the statistical ensemble $\{N_{ch}nVT\boldsymbol{\mu}^*\boldsymbol{\alpha}\}$. The well-known end-bridging Monte Carlo move was included to help drive the system to the steady state for each value of α_{xx}. Other MC moves, in addition to the end-bridging move (50%), for rigorous phase-space sampling were the reptation (10%), the end-mer rotation (2%), the flip (6%), and the concerted rotation (32%) moves.

A small polydispersity (~1.083) was imposed in conjunction with the end-bridging move. As explained in detail by Pant and Theodorou [34], the chain-length distribution as well as the polydispersity in conjunction with the connectivity-altering, end-bridging MC algorithm can be controlled by adjusting the spectrum $\boldsymbol{\mu}^*$ of the chain relative chemical potentials in a semi-grand ensemble, as quantified by Eq. (2). Pant and Theodorou presented analytical expressions for $\boldsymbol{\mu}^*$ that reproduce the three most common molecular weight distributions: the uniform distribution, the Gaussian distribution, and the most probable distribution. In this study, we chose the uniform distribution in a pre-specified interval around the mean chain length ($C_{78}H_{158}$), since this distribution has been successfully applied in many previous works for various polymeric systems: e.g., Refs. [29–31] for bulk linear polymers, Daoulas et al. [35] for grafted chain systems, and Baig et al. [36] for branched polymers. The uniform distribution of the chain length, whose mean value is N in the chain-length interval between

$N(1-X)$ and $N(1+X)$, is achieved by setting $\boldsymbol{\mu}^*$ such that $\mu_k^* = 0$ for $N(1-X) \le k \le N(1+X)$ and $\mu_k^* = -\infty$ otherwise. The polydispersity index I is then controlled by choosing the parameter X; e.g., for $X = 0.5$, $I \approx 1.083$, as was selected in this work.

A broad range of α_{xx} values, [0.05,1.0], was applied to the fluid simulations, in addition to the quiescent condition ($\alpha_{xx} = 0.0$). As a physical reference point, an empirical relation between $\boldsymbol{\alpha}$ and the Weissenberg number, *Wi* (defined as the product of the strain rate and longest relaxation time of the fluid), for three different chain-length liquids ($C_{50}H_{102}$, $C_{78}H_{158}$, and $C_{128}H_{258}$) under shear flow was reported in Ref. [31] by comparing the conformation tensor $\tilde{\mathbf{c}}$ obtained in NEMC with the NEMD results under shear flow reported by Kim et al. [37]. For the $C_{78}H_{158}$ melt examined in these simulations, the longest relaxation time is known to be approximately 2.3 ns [38]. A similar procedure was applied in this work to estimate the range of *Wi* values corresponding to the range of α_{xx} values stated above and the same temperature and density; however, in the present case, the NEMC simulations were of uniaxial elongational flow whereas the NEMD simulations of Refs. [37,39] were of planar elongational flow. (Note that uniaxial elongational flow cannot be examined in a traditional NEMD simulation because of the lack of an appropriate set of boundary conditions [40].) Therefore, this comparison was made mainly using the stretching component of the conformation tensor, $\tilde{c}_{xx}$, which appears to be very similar between the two cases. According to this procedure, the estimated range of Weissenberg number applied in this study is roughly corresponding to $0.1 \le Wi \le 200$.

The liquid studied in this work consisted of 160 linear $C_{78}H_{158}$ molecules and was maintained at four different temperatures and a constant density of $\rho = 0.7638\,\mathrm{g/cm^3}$. A relatively large rectangular box with dimensions of $130.5 \times 54 \times 54$ ($x \times y \times z$) Å^3 was chosen to minimize the system-size effects (especially under strong flow fields), based on the maximum chain length $|R|_{\max} = 99.4$ Å; i.e., with the equilibrium C–C bond length (1.54 Å) and C–C–C bending angle (114°) in the all *trans*-conformation. The mean chain end-to-end distance at equilibrium is $\left\langle R^2 \right\rangle_{eq}^{1/2} = 39.3 \pm 0.5$ Å at $T = 450$ K. Therefore, the x-dimension of the simulation box was at least 30% larger than $|R|_{\max}$, and similarly for the y and z dimensions compared to $\left\langle R^2 \right\rangle_{eq}^{1/2}$. The atomistic interactions within the melt were described using the well-known SKS (Siepmann–Karaboni–Smit) potential model [41], which has been widely used for simulating n-alkane systems at equilibrium and their nonequilibrium states under flow [27,30,31,39,42]. This model consists of four types of energetic interactions between united-atom sites, each considered to represent the respective carbon atoms and its attached hydrogen atoms. The bond-bending energy quantifies the energetic interactions between atoms separated by one adjacent atom. It is expressed as a harmonic potential function around an equilibrium bond angle of 114°. The bond-torsional energy quantifies the energy of atoms separated by three bonds, and is expressed in terms of a cosine power series. The intramolecular Lennard–Jones (LJ) energy quantifies interactions between atoms on the same chain that are separated by four or more bonds, where as the intermolecular LJ energy represents interactions between atoms on separate chains. The distance between adjacent atomic units is held fixed at 1.54 Å. Exact expressions for all of these energies can be found in the literature [27,30,31,39,41,42].

In the present work, a fully equilibrated configuration was first prepared under equilibrium conditions ($\alpha_{xx} = 0$) for each temperature. This well-equilibrated system configuration was subsequently employed as the initial configuration in the NEMC simulations for all nonequilibrium states at each temperature, although it might be more efficient to use a pre-deformed configuration obtained from the lower values of α_{xx} as the initial configuration for the simulations of higher α_{xx} values; however, the technique employed here mimics more closely the actual experiment where a constant strain rate is applied instantaneously to a quiescent sample. In addition, we report that the computational time to reach the steady-state was almost independent of the imposed field strength; this contrasts with the well-known fact [39,42] that NEMD simulations generally require more time to achieve the steady-state as the field is weaker. (This can be considered as an additional advantage of NEMC method over NEMD.) Note that the conventional periodic boundary conditions were equally applied to all three (x, y, and z) directions in all simulations so that there should not be any geometric effect on the physical properties reported in this study.

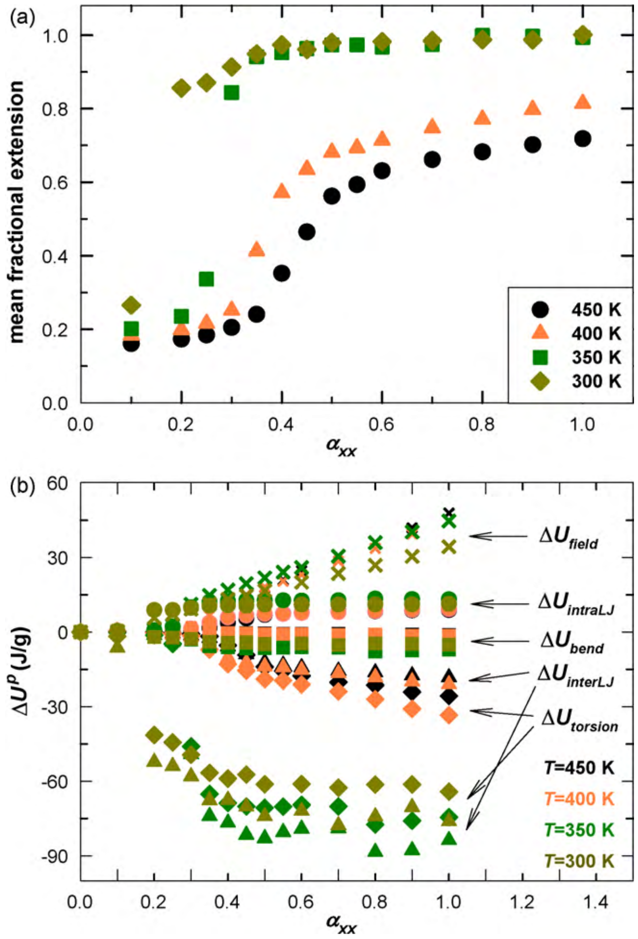

Fig. 1. (a) Mean fractional chain extension $\left\langle R^2 \right\rangle / \left\langle R^2 \right\rangle_{\max}$ and (b) each potential energy change (relative to equilibrium states) with respect to the field strength: ΔU_{bend}, bond-bending; $\Delta U_{torsion}$, bond-torsional; $\Delta U_{interLJ}$ and $\Delta U_{intraLJ}$, intermolecular and intramolecular Lennard–Jones, respectively; ΔU_{field}, field energy ($= N_{ch} k_B T \boldsymbol{\alpha} : \tilde{\mathbf{c}}$).

3. Results and discussion

3.1. Chain configuration and potential energies

The effects of the flow field on the overall chain configuration are presented in Fig. 1a in terms of the mean-fractional chain extension (as in Ref. [28]), which is calculated as the ratio of the average chain extension relative to the maximum chain length, $\langle R^2 \rangle / \langle R^2 \rangle_{\max}$. Although the mean-fractional extension monotonically increases with the flow strength for all liquids, a clear distinction is noticed between the liquids at the higher two temperature values and those at the lower temperatures; that is, while the systems at $T = 400$ and 450 K exhibit sharp but continuous changes (indicating a smooth transition from the coiled to the stretched configuration), abrupt and discontinuous transitions (very close to the maximum attainable value of unity) were observed at distinct values of critical flow strength in the liquids at $T = 300$ ($\alpha_{xx} = 0.2$) and 350 K ($\alpha_{xx} = 0.3$). This observation supports the concept of the "coil-stretch transition" hypothesized by de Gennes [43]. These results are indicative of the possibility that there are distinct differences between the morphologies of the liquids at the lower and higher temperatures. Furthermore, when the flow field is suddenly turned off ($\alpha_{xx} = 0.0$), the higher temperature liquids (as well as the lower temperature liquids below their respective critical value of flow strength) rapidly return to the conditions of the quiescent melts, whereas the lower two temperature liquids, above their respective critical flow strength, maintain their steady-state values of the mean fractional extension out to 2 billion MC steps (see Fig. 2 of Ref. [28]). This indicates that some permanent change has occurred within the samples at lower temperatures, and that a solid-like phase has been formed. Also note that the chain configurations at the lower two values of temperature are essentially fully extended (i.e., with all bond-torsional angles in *trans* conformations), whereas the higher temperature liquids exhibit configurations of at most 80% extension.

Fig. 1b displays the flow-induced changes of each type of potential energy relative to its equilibrium value with respect to the flow strength. At all temperatures, it is observed that as the flow strength increases, (a) the field ($\Delta U_{field} = N_{ch}k_BT\,\boldsymbol{\alpha} : \tilde{\mathbf{c}}$) and the intramolecular Lennard–Jones (LJ) ($\Delta U_{intraLJ}$) energies increase, (b) the bond-torsional ($\Delta U_{torsion}$) and intermolecular LJ ($\Delta U_{interLJ}$) energies decrease, and (c) the bond-bending energy (ΔU_{bend}) only slightly decreases.

First, we notice that for all temperatures the bond-bending energy appears to decrease as the field strength increases (although the change is relatively minor, indicative of a slight variation in the bending angles with the field). More importantly, the magnitude of the decrease is seen to be larger for the lower temperature systems than the higher temperature systems; this seems to indicate more significant changes in the bending angle distributions at the lower temperatures. In order to understand these phenomena in more detail, we present in Fig. 2 the probability distribution function of the bond-bending angle θ at equilibrium and nonequilibrium states. Under equilibrium conditions (Fig. 2a), the distribution becomes narrower with a higher value of the peak around the equilibrium angle (114°) as the temperature is decreased; this is physically reasonable since the thermal fluctuations of the bending angle generally increase with increasing temperature, as is also expected from the Boltzmann distribution [e.g., Eq. (2)]. Fig. 2b displays the distribution functions at $\alpha_{xx} = 1.0$, where the overall results appear to be very similar to those at equilibrium. However, significantly distinctive features between the lower and higher temperature systems appear when looking at the differences between the equilibrium and nonequilibrim distribution functions, as depicted in Fig. 2c. At the higher temperatures (400 and 450 K), there appear positive peaks for $114^\circ \le \theta \le 130^\circ$ and minima for $95^\circ \le \theta \le 114^\circ$, thus leading to a slight increase in the average value of the bond-bending angle; this further indicates an asymmetric angle distribution function at high fields, contrasting the perfectly symmetric Gaussian distribution at equilibrium. In sharp contrast, at the lower temperatures (300 and 350 K), it is seen that the distribution function increases symmetrically around the equilibrium angle ($107^\circ \le \theta \le 121^\circ$), whereas it decreases outside this range; this result indicates the overall much narrower distribution function at $\alpha_{xx} = 1.0$ compared to equilibrium, signifying a flow-induced crystalline structure. (Further evidence is presented in the bond-torsional energy and the corresponding distribution, below.)

The bond-torsional energy decreases with increasing flow strength, in accordance with the notion that the chain configurations become more *trans*-oriented with increasing flow strength. The trend with temperature is quite dramatic: at the higher two values of temperature, the torsional energy change is much less significant than at the lower temperatures, and there is an abrupt transition at the lower temperatures at the critical values of α_{xx} mentioned above. This trend is in agreement with the mean-fractional extensions of Fig. 1a. Detailed information can be obtained by looking into the torsional angle distribution $P(\phi)$, which is presented in Fig. 3. At equilibrium (Fig. 3a), the overall shapes of $P(\phi)$ look similar to each other between different temperatures; evidently, however, the relative extent of the *trans*-conformation becomes larger as the temperature is decreased, as consistent with the theoretical predictions of the Boltzmann distribution. By comparison, when a very strong field is applied to the systems, the

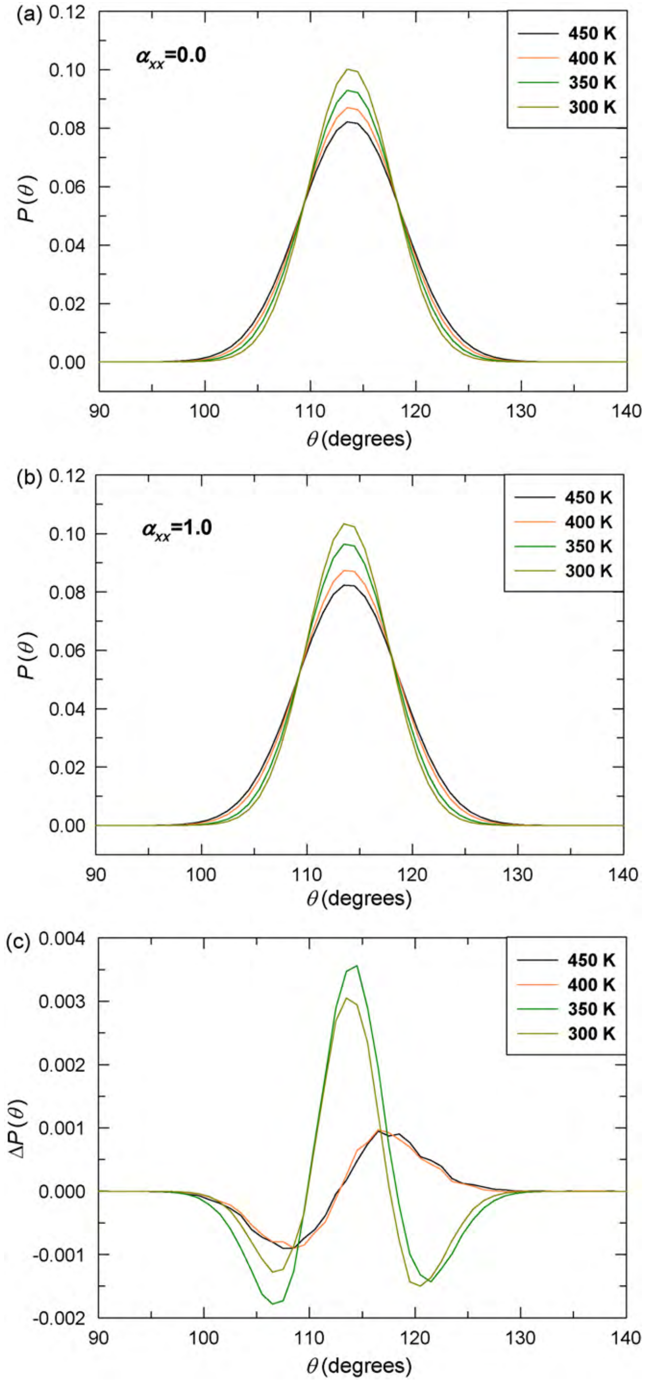

Fig. 2. Probability distribution function $P(\theta)$ of the bond-bending angle θ of the simulated systems under (a) equilibrium conditions ($\alpha_{xx} = 0.0$), (b) subjected to the flow strength $\alpha_{xx} = 1.0$, and (c) $\Delta P(\theta) \equiv P(\theta)\big|_{\alpha_{xx}=1.0} - P(\theta)\big|_{\alpha_{xx}=0.0}$.

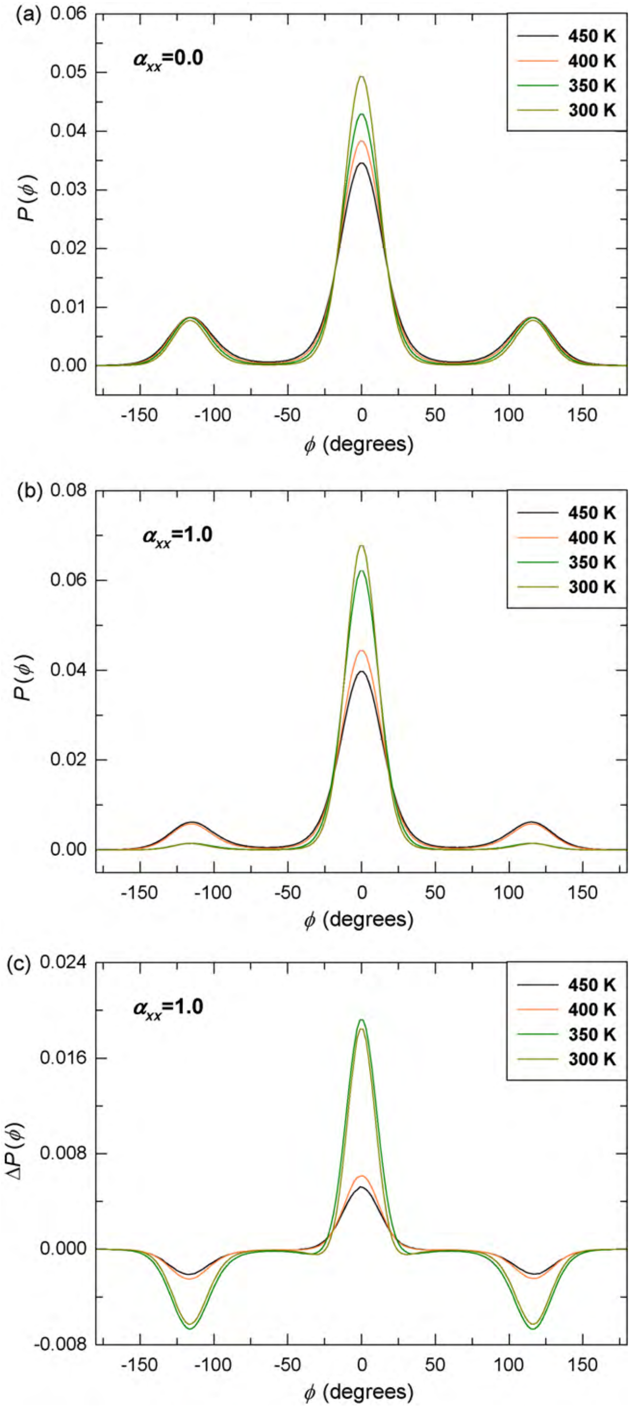

Fig. 3. Probability distribution function $P(\phi)$ of the bond-torsional angle ϕ of the simulated systems under (a) equilibrium conditions ($\alpha_{xx} = 0.0$), (b) subjected to the flow strength $\alpha_{xx} = 1.0$, and (c) $\Delta P(\phi) \equiv P(\phi)\Big|_{\alpha_{xx}=1.0} - P(\phi)\Big|_{\alpha_{xx}=0.0}$.

rather smooth variation of $P(\phi)$ with temperature at equilibrium states appears to break down, as shown in Fig. 3b. It is evident in the figure that the distribution function of the *trans*-state is increased relative to its equilibrium value for the higher temperature systems, which is accompanied by a depletion of the distribution function of the *gauche*-state, as more clearly seen in Fig. 3c. Furthermore, the increase of the *trans*-state is somewhat higher for $T = 400$ K than $T = 450$ K, as consistent with the results shown in Fig. 1a. In contrast, the distribution function for the lower temperature systems exhibits a significant increase in its value at the *trans*-state, accompanied by the large depletion of the *gauche*-state (see Fig. 3b and c); this result supports the hypothesis of the development of flow-induced crystalline in the lower temperature systems.

The intramolecular LJ energy change increases with increasing flow strength and with decreasing temperature. This means that this LJ energy becomes less negative with increasing flow strength, signifying a larger separation between atoms separated by more than three bonds along the chain. This is to be expected as the chains extend their configurations with increasing α_{xx}. Also, the trend with respect to temperature is also consistent with the trend in chain extension with decreasing temperature values by the same reasoning. The intermolecular LJ energy offers insight into the interactions between atomic units on separate chains, and therefore provides crucial information regarding the long-range structural properties of the liquids. The decrease in the intermolecular LJ energy is indicative of a closer packing between atomic units on different chains, implying that the molecules are orienting self-consistently into lower energy structures on the super-atomic scale. This LJ energy change is very dramatic at the lower two values of temperature, and discontinuous at the critical values of α_{xx} mentioned above. Hence the intermolecular LJ energy is a major factor in any long-range structure that is forming under these conditions.

3.2. Pair correlation function and structure factor

Detailed local and global structural changes experienced by the liquids can be analyzed by examining the pair correlation function $g(r)$ and structure factor $S(k)$, which is the Fourier transform of $g(r)$. Plots of the total pair correlation for all four temperature values are presented in Fig. 4. This quantity is essentially independent of temperature under equilibrium conditions, displaying the characteristic liquid structure of short-chain alkanes (Fig. 4a). The two large peaks at 1.54 and 2.58 Å represent the atom bound to the reference atom and the atom one bond unit away from it; i.e., the rigid bond between two atoms and the distance from the atom forming the backbone bond angle between atoms separated by another atom. The other peaks represent the atomistic positions of *n*-alkane liquids corresponding to the *gauche*- and *trans*-conformations, and so on (see Ref. [27] for a more detailed description of this characteristic peak structure).

The experimental melting point of polyethylene crystals is reportedly around 380 K at atmospheric pressure [44]. In this respect, it is apparent that the two lower temperature liquids, at 300 and 350 K, are already below the experimental melting temperature; however, simulations were run for several billion MC steps for these two liquids, with no resulting change in the systems' configurational properties under quiescent conditions ($\alpha_{xx} = 0.0$). Were the simulations long enough, it should nevertheless be possible for these liquids to overcome the free energy barrier to enable crystallization at equilibrium; however, this does not detract from the point herein that the effective free energy barrier is effectively, and significantly, lowered by the application of a uniaxial flow field of sufficient strength. (This issue will be discussed further in subsequent subsections.)

At the field strength $\alpha_{xx} = 1.0$, the liquids at the higher two temperature values retain their liquid-like characteristics, with essentially the same features for large distances (>8 Å) as the equilibrium case. However, for short-range distances (<8 Å), the behavior is quite different from the equilibrium case, and corresponds to chain configurations that are highly extended with respect to the random coil configurations at $\alpha_{xx} = 0.0$. (There differences are difficult to resolve between Fig. 4a and b, but can be discerned easily in Fig. 2a of Ref. [27], where a detailed discussion may be found.)

The lower two temperature liquids display a very different behavior for $\alpha_{xx} = 1.0$. The short-range chain configurations display the same qualitative features as those of the higher tem-

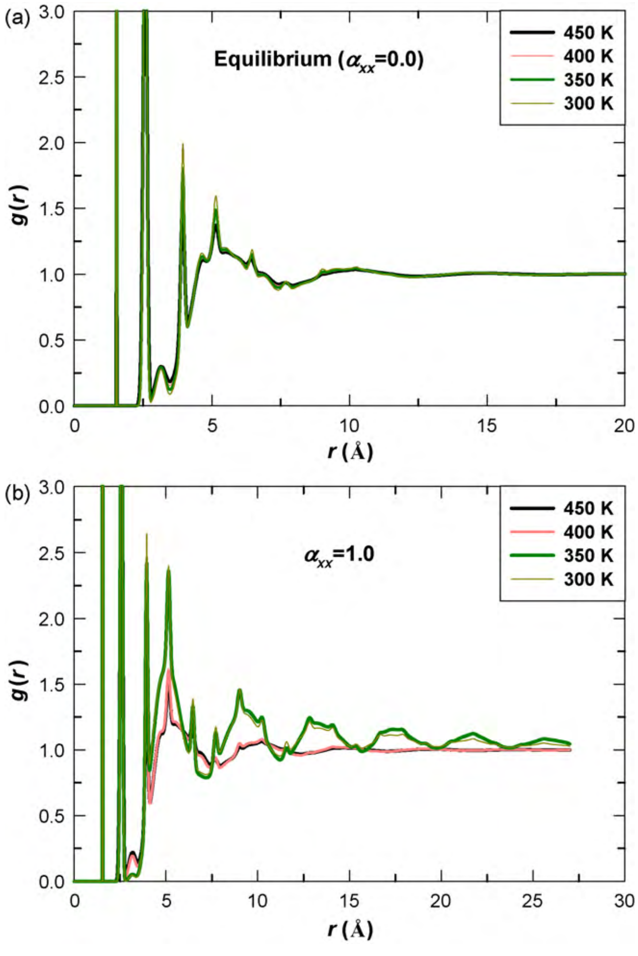

Fig. 4. Pair distribution function $g(r)$ of the simulated systems under (a) equilibrium conditions and (b) subjected to the flow strength $\alpha_{xx} = 1.0$.

peratures, only more pronounced, thus indicating even more highly-extended configurations than in the higher temperature fluids (consistently with Fig. 1a). However, the lower temperature liquids exhibit a distinct long-range structuring patterning that occurs out to the limitation imposed by the simulation box, which is 27 Å.

The effect of the flow field on the intermolecular contribution to $g(r)$ is displayed in Fig. 5a (see also Fig. 1 of Ref. [28]). (For comparison, the corresponding equilibrium data are presented in the inset). In contrast to the relatively small enhancement of fluctuations in the local packing density exhibited at T = 400 and 450 K, distinctively large and long-range periodic fluctuations (even extending beyond the maximum distance allowed by the box dimensions) are observed in the liquids at 300 and 350 K. According to the general rule of thumb for amorphous polymers [45], a significant degree of crystalline structure has developed when the periodic character exists out to roughly 25 Å. It is thus evident that a semi-crystalline phase has developed in the lower temperature liquids at high values of field strength. Note that at 400 and 450 K, the periodicity has almost decayed by r = 15 Å, indicating the lack of a long-range order in the liquids; however, it does imply that the local, short-range chain configurations are highly extended relative to their equilibrium configurations, although not to the same degree as for the lower temperature liquids.

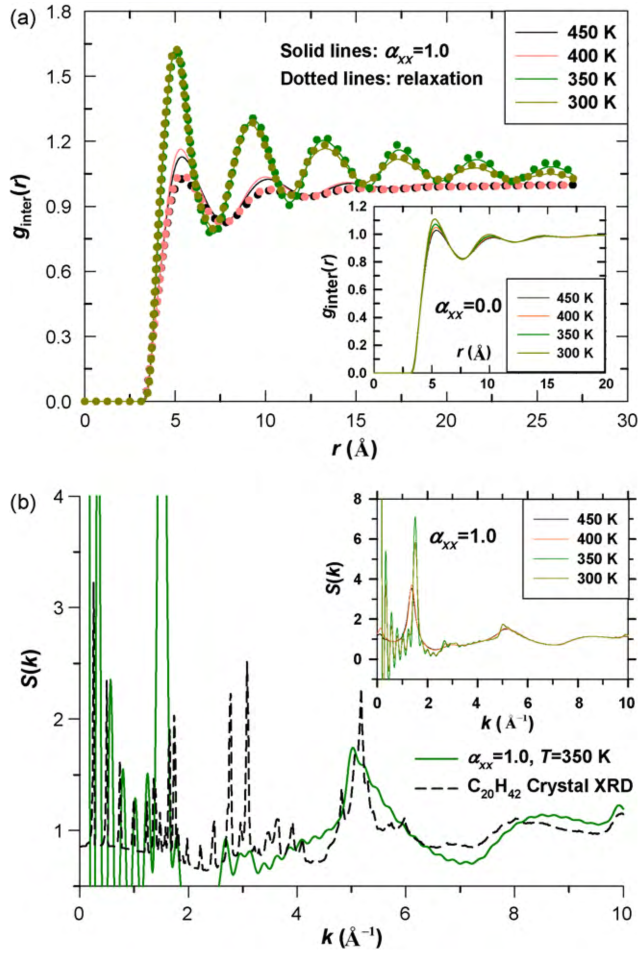

Fig. 5. (a) Steady-state intermolecular pair distribution function $g_{\text{inter}}(r)$ of each system subjected to the field strength of $\alpha_{xx} = 1.0$ (solid lines) and under a fully relaxed condition after turning off the field (dotted lines). The inset shows $g_{\text{inter}}(r)$ at equilibrium for each value of temperature. (b) Comparison of the structure of the flow-induced crystalline phase developed in the liquid at $T = 350$ K with the X-ray diffraction experimental data of a n-eicosane crystal [27]. The inset shows the simulation data at $\alpha_{xx} = 1.0$ for each value of temperature.

Further supporting evidence for the existence of a stable FIC phase at the lower values of temperature is provided by examining the relaxation behaviors of the liquids after turning off the applied field, as mentioned above. It is evident that whereas the systems at 400 and 450 K have returned back to their equilibrium structures after cessation of flow, the long-range ordered structures of the FIC phases created at T = 300 and 350 K remain without disruption, at least through two billion MC steps.

From a thermodynamic perspective, this result indicates that the free energy barrier existing between the equilibrium melt phase and the FIC phase at the lower temperatures is so high as to make the transition between the two phases very difficult within a reasonable amount of time. The system would likely reach the isotropic equilibrium melt phase after a sufficiently long time, and the relative residence time between the FIC and isotropic equilibrium states would depend on the ratio of their respective free energy values, based on the Boltzmann distribution. Analogously, if we keep performing the MC simulations of the system at the FIC phase with turning off the field for a very long time, the system might possibly eventually overcome the high free energy barrier and reach the original equilibrium melt state; however, this seems to be very unlikely given that the temperature (300 or 350 K) is far below the quiescent melting point of 380 K. Again, the important point is that the FIC phases induced at the lower temperatures are very stable so as not to be easily destroyed even after turning off the flow field for a significant amount of time. (Refer also to Fig. 2 in Ref. [28], where the relaxation behaviors of the systems were depicted more directly in terms of the evolution of the mean chain end-to-end distance after switching off the flow for two billion MC steps.)

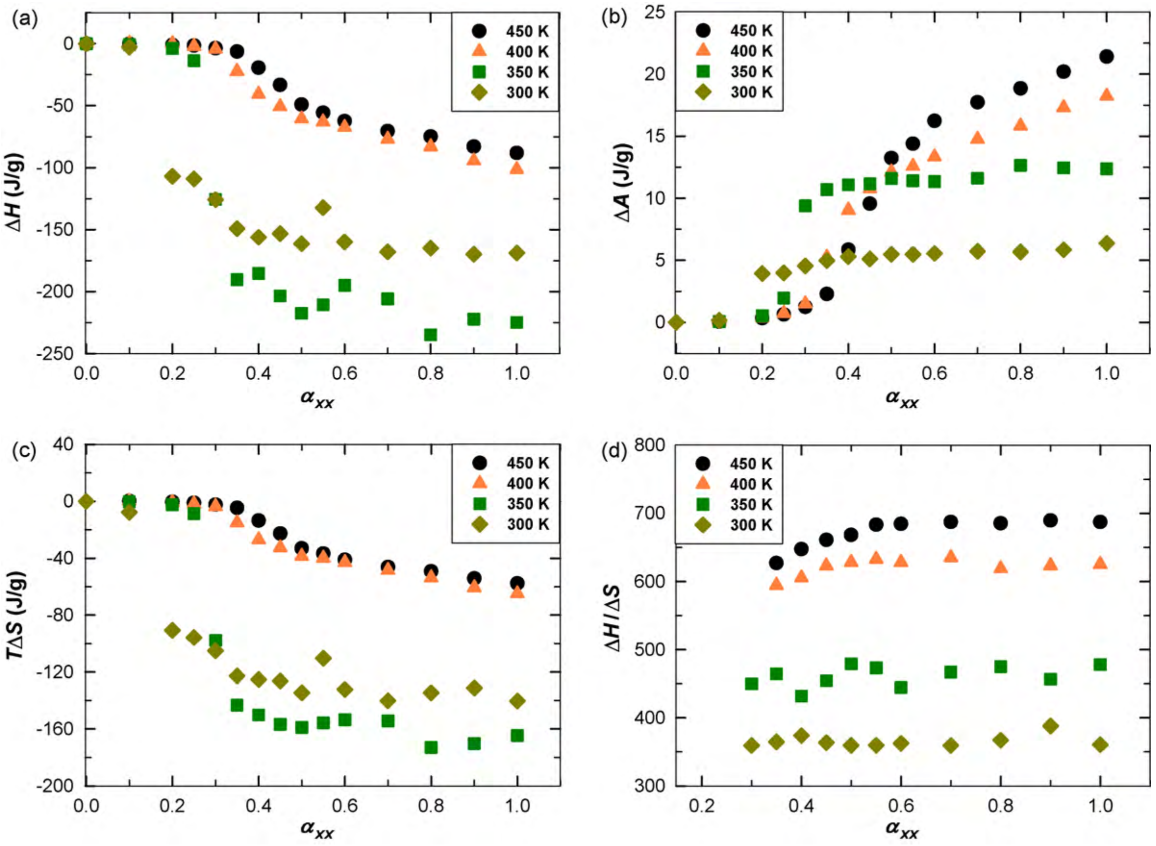

Fig. 6. Thermodynamic functions at nonequilibrium states (relative to equilibrium states) as a function of the field strength: (a) enthalpy, (b) Helmholtz free energy, and (c) entropy. The standard errors are commensurate with the size of the symbols.

The structure factor, $S(k)$, is displayed in Fig. 5b. Highly anisotropic structures were observed at all temperature values under a strong flow field (inset, Fig. 5b), as evident from the shift in the first and second major peaks at high k values ($> 1.4\,\text{Å}^{-1}$) from their equilibrium structures. (This point is more easily recognizable in Fig. 2b of Ref. [27].) At 400 and 450 K, however, no long-range crystalline order was detected at low values of k, indicating that, although the molecules were dramatically oriented and stretched under flow, no flow-induced crystallization had occurred. In sharp contrast, for the systems at $T = 300$ and 350 K, distinct Bragg peaks at small k ($<1.5\,\text{Å}^{-1}$) were evident, associated with the development of a long-range order, typical of a real crystal. Additional features supportive of the FIC phase were the shift of the main peak at $k \approx 1.38\,\text{Å}^{-1}$ occurring in equilibrium melts to larger $k \approx 1.52\,\text{Å}^{-1}$ (indicating a closer lateral packing between neighboring chains) and the broken symmetry of the peak at $k \approx 5\,\text{Å}^{-1}$.

The structure factor of the flow-induced crystal bears a striking resemblance to that of a quiescently crystallized sample. The main graph in Fig. 5b displays data for the structure factor of the simulated flow-induced crystal at 350 K and $\alpha_{xx} = 1.0$ in comparison to experimental x-ray diffraction data of a similar n-eicosane crystal, $C_{20}H_{42}$, indexed as triclinic, from Ref. [27]. A remarkable quantitative match is seen for the Bragg peaks below $k = 1.4\,\text{Å}^{-1}$, confirming the existence of regular intermolecular crystal planes in the FIC phase, as well as above $6\,\text{Å}^{-1}$, indicating intramolecular configurations similar to those in the actual crystal. In the intermediate range, $2<k<6\text{Å}^{-1}$, the two distinct crystalline Bragg peaks at 2.7 and $3.1\,\text{Å}^{-1}$ are much less pronounced in the simulation data, indicating that the FIC phase has a slightly different morphology than the quiescently crystallized sample, which is consistent with experiment [2,4–7]. These peaks occur roughly at a length scale of 2.1 Å ($2\pi/k$), indicating a distinct probability that they are associated with the lateral (with respect to the direction of chain extension) packing of the linear macromolecules. This mismatch in the height of the Bragg peaks might be due to the assumption of constant density in the simulations, which does not allow volume changes upon crystallization that might have appeared in simulations at constant pressure. (This issue will be discussed further below.) Another possibility is that this difference arises due to innate differences between the n-eicosane sample examined experimentally and the $C_{78}H_{178}$ fluid studied via simulation; i.e., the smaller chain molecules of n-eicosane might allow for a tighter packing due to a lower entropic configurational effect. A further possibility is that this discrepancy might arise due to differences between configurational entropies as induced by flow, rather than molecular size; i.e., differences solely due to flow-induced, rather than quiescent, crystallization.

3.3. Enthalpy, Helmholtz free energy, and entropy

Fundamental extensive thermodynamic quantities can be determined from the simulation output as functions of the applied flow strength, such as enthalpy, Helmholtz free energy, and entropy. The enthalpy changes, ΔH [as expressed by the Legendre transformation $\Delta U + \Delta(PV)$], associated with specified values of α_{xx} for the four temperature liquids are displayed in Fig. 6a. At the lower two temperatures, there is again a large and discontinuous change in the enthalpy of the FIC phase at the critical flow strengths relative to the equilibrium states, which contrasts with a relatively small and smooth change at the higher two temperatures. As an interesting point, we note that the value of ΔH at $\alpha_{xx} = 1.0$ (~225 J/g) at 350 K is remarkably close to the experimental heat of fusion (276 J/g) of a polyethylene crystal under quiescent conditions [44].

Fig. 6b presents the Helmholtz free energy change, ΔA, with respect to the field strength, which has been calculated via thermodynamic integration using

$$\Delta A \equiv A(T, V, N_{ch}, N_{ch}\tilde{\mathbf{c}})\big|_{\boldsymbol{\alpha}} - A(T, V, N_{ch}, N_{ch}\tilde{\mathbf{c}})\big|_{\boldsymbol{\alpha}=0}$$

$$= N_{ch}k_BT\left(\boldsymbol{\alpha} : \tilde{\mathbf{c}} - \int_0^{\boldsymbol{\alpha}} \tilde{\mathbf{c}} : d\boldsymbol{\alpha}\right), \qquad (8)$$

as derived using Eqs. (7a) and (7b). In the special case of uniaxial elongational flow represented by Eq. (4), ΔA is calculated as

$$\Delta A = N_{ch}k_BT\left\{\alpha_{xx}\left(\tilde{c}_{xx} - \frac{1}{2}\tilde{c}_{yy} - \frac{1}{2}\tilde{c}_{zz}\right) - \int_0^{\alpha_{xx}}\left(\tilde{c}_{xx} - \frac{1}{2}\tilde{c}_{yy} - \frac{1}{2}\tilde{c}_{zz}\right)d\alpha_{xx}\right\}. \quad (9)$$

It is evident from the figure that at the lower two temperature values, the free energy exhibits a sudden increase at the critical flow strengths and reaches an asymptotic value that is smaller at the lower values of temperature (300 and 350 K). In contrast, for the higher two temperature liquids, ΔA increases continuously with the flow strength, without attaining an asymptotic value. ΔA is observed to be larger for the higher temperature system, both liquid (450 K) and FIC (350 K). Since in view of thermodynamics the higher free energy represents the less stable state, the relatively small change of ΔA at $T = 300$ and 350 K indicates that the FIC phase created under strong flow fields is a quite stable thermodynamic state compared to the original equilibrium state; accordingly, the oriented melt phase at 400 or 450 K is a relatively unstable state, and should disappear after removal of the flow field. This interpretation is also consistent with the relaxation simulation result shown in Fig. 5a.

Another way to interpret this data is by consideration of the liquids' entropy changes with respect to flow strength, as presented in Fig. 6c. The behavior of ΔS [as obtained from $(\Delta U - \Delta A)/T$], is qualitatively similar to that of ΔH, with discontinuous changes at the critical values of α_{xx} for the liquids at the lower two values of temperature. The Legendre transformation of the Helmholtz energy, $\Delta A = \Delta U - T\Delta S$, indicates that the change in Helmholtz energy depends on the changes in both internal energy and entropy. It is evident from the simulation results of Fig. 1b that the energy change for the lower two temperature liquids is much more significant than at the higher two temperatures. This relatively large change in the internal energy offsets the large change in the entropy of the liquids at lower temperatures, leading to ΔA vs. α_{xx} curves that decrease in magnitude with decreasing temperature. The primary contributor to this large change in internal energy is the intermolecular LJ energy (see Fig. 1b). Hence it is the molecular packing, and not the individual chain configurations (an entropic effect), that drive the crystallization event.

In conjunction with the thermodynamic expression for the equilibrium melting temperature during a phase transition ($T_m = \Delta H/\Delta S$), we plot $\Delta H/\Delta S$ vs. α_{xx} in Fig. 6d (only the statistically meaningful data are included). For the higher temperatures, the ratio appears to increase and then reach an asymptotic value at high values of α_{xx}, whereas for the lower temperatures it exhibits small fluctuations around a constant value beyond $\alpha_{xx} = 0.25$ approximately the critical value of this quantity. (This is physically consistent with the behavior of ΔA in Fig. 6b.) Overall, the asymptotic value for each temperature is observed to be larger than the set temperature; approximately 50–55% for $T = 400$ and 450 K, and 20–35% for $T = 300$ and 350 K. At the higher two temperatures, where no crystallization is occurring, the association between $\Delta H/\Delta S$ and T_m is meaningless. However, at the critical values of α_{xx} of the lower two temperature liquids, it is possible that this significant enhancement in the set point temperature is in some way correlated with a rise in the quiescent melting point for the FIC phase. Note that for the lower temperatures where an FIC phase is created, the ratio ($\Delta H/\Delta S$) may be thermodynamically related to the equilibrium melting temperature at constant pressure (e.g., $P = 1$ atm) instead of the fixed density imposed in the present simulations. (This issue will be further discussed below.)

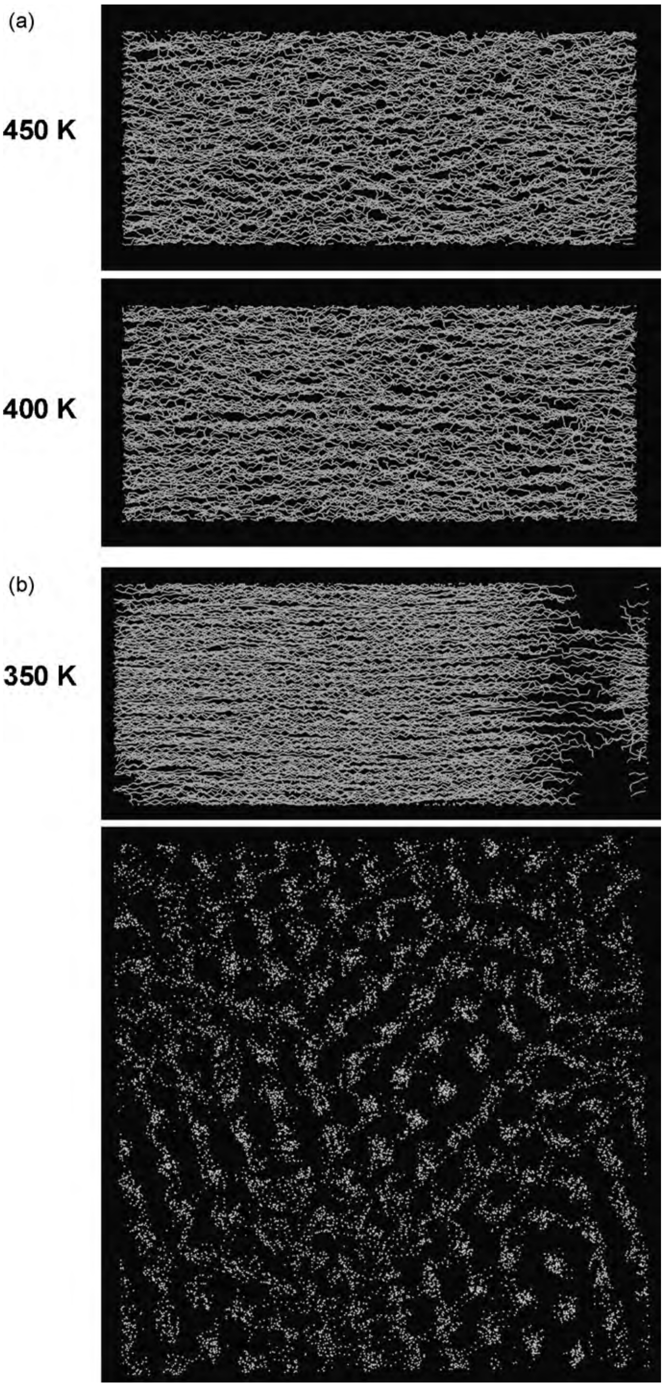

Fig. 7. Representative atomistic snapshots of (a) the oriented melt phase produced under $\alpha_{xx} = 1.0$ at $T = 450$ K (top panel) and $T = 400$ K (bottom panel) and (b) the FIC phase created under $\alpha_{xx} = 1.0$ at $T = 350$ K. In order to visualize the structural arrangements of the chains in the FIC, the coordinates of each atom in the system are projected to the *yz*-plane in the bottom panel of (b).

3.4. Visualization of crystalline structure

Fig. 7 depicts instantaneous snapshots to help compare the oriented melt structure occurring under $\alpha_{xx} = 1.0$ at the higher temperatures (Fig. 7a) with the FIC structure created under $\alpha_{xx} = 1.0$ at $T = 350$ K (Fig. 7b). For the system at $T = 450$ K (top panel, Fig. 7a), although chains are seen to be generally oriented with respect to the flow (x) direction, there appears no clear signature for crystalline structure, both locally and globally. Although a qualitatively similar image is exhibited by the system $T = 400$ K (bottom panel, Fig. 7a), here the chains are observed to be much more oriented with respect to the flow direction, and better aligned to each other. More importantly, by looking closely at the picture, one can observe certain local packing between chains scattered in space alongside with some degree of spatial inhomogeneity; this is considered as a precursor for the development of crystalline structure, which disappears after the field is turned off ($\alpha_{xx} \to 0.0$); refer to Fig. 2 of Ref. [28]. A well-defined crystalline structure is eventually developed at the lower temperature (350 K), as is evident from Fig. 7b (top panel) where each chain is highly stretched with practically all *trans*-conformations in the x-direction. Furthermore, there appears to be a regular layer-by-layer arrangement between chains in the y-direction. In order to see more clearly such a structural arrangement of the chains, the coordinates of each atom are projected onto the yz-plane of the system, as displayed in the bottom panel of Fig. 7b where the atoms belonging to the same chain appear as a group in most chains, although some chains show a significant degree of scatter. Most notably, a certain hexagonal arrangement of the molecules is quite evident in the figure, indicative of a crystalline structure. No such regular array structure was found in the highly oriented melts under $\alpha_{xx} = 1.0$ at $T = 400$ and 450 K.

Another interesting feature of Fig. 7b is the low population density of molecules on the right side of the simulation box. (Note that no such inhomogeneity is observed for the systems under $\alpha_{xx} = 1.0$ at $T = 400$ and 450 K, indicating that such spatial inhomogeneity in density is not due to the periodic boundary conditions applied in the simulations.) This might be an indication of a precursor to a smectic phase-like ordering at high field strengths, but it is more likely an effect arising from the constant density simulations; i.e., in order to have a crystallization event, the density of the material must decrease, packing the same number of molecules into a smaller volume. Therefore, to accomplish this, there is a region of low density at the right end of the simulation box. It is also evident that the molecules within this low-density region are not as well-oriented as in the dense portion of the cell. By excluding the less dense region of the simulation box from a density calculation, the bulk density of the dense region increases from the preset value of 0.764 g/cm^3 to 0.913 g/cm^3. This higher value is close to the experimental range for n-alkanes with backbones composed of 21–40 carbon units, 0.93–0.95 g/cm^3 [46].

Longer, entangled polyethylenes will form semi-crystalline fibers in shish-kebab structures, where crystalline regions with high densities are separated by less oriented strands of amorphous polymer with lower densities. This visualization might provide clues into this process. In addition, the $C_{78}H_{158}$ PE melts employed here consist of relatively short chains compared to the polymers usually encountered in industrial processes. Therefore, it is not surprising to observe that almost entire portion of each chain can be stretched as well as oriented with respect to the flow direction under strong flows, thus leading to more fully crystalline structure. If the chains were long enough, one would expect a variety of crystalline structures (shish-kebab, spherulitic, etc.) depending on the field strength at specific temperatures and entanglement density of the chains, as typically observed in real experiments. In addition, as the crystalline morphology can be very sensitive to the field strength, especially at very high fields, if an enormously strong external field is applied to the system, strictly shish-like crystalline structures can develop even in long entangled polymer melts, similar to the FIC found in the present study. Note that the spatial inhomogeneity appearing in the FIC occurring in the lower temperature systems may affect to some extent the overall results of $g(r)$ or $S(k)$; however, their portions are observed to be relatively small compared to the entire crystalline domain so that the general results and conclusions presented above are expected to be unaffected. Future work will explore this effect in more detail by performing variable density NEMC simulations at constant pressure, perhaps using a bigger simulation box in order to remove any possible artifacts from the system size or periodic boundary conditions.

3.5. *Configurational temperature*

Traditionally, temperature is a thermodynamic quantity that is directly related to the momentum or kinetic energy of atoms. Rugh [47,48] discovered that the system temperature can be calculated from a geometric structure of the energy surface of the system using the fundamental thermodynamic relation of temperature ($1/T = \partial S/\partial E$) and the statistical expression of entropy $S_E = k_B \ln[\int \delta(H(\Gamma) - E) d\Gamma] + C$ for an isolated system with the Hamiltonian, H, being equal to the energy, E. In this expression, C is a constant and $\mathbf{\Gamma}$ represents the phase space consisting of all the positions $\{\mathbf{r}\}$ and momenta $\{\mathbf{p}\}$ of the particles in the system. Starting from the microcanonical statistical ensemble, Rugh derived the following fundamental equation for the temperature

$$\frac{1}{k_B T} = \left\langle \nabla \cdot \left(\frac{\nabla H}{\left|\nabla H\right|^2} \right) \right\rangle, \tag{10}$$

where the angular brackets represent an ensemble average, and the gradient vector involves all the degrees of freedom in $\mathbf{\Gamma}$. It is thus seen that the system's temperature is directly associated with the intrinsic structure of the energy surface of the system. A further generalization of Rugh's discovery by Evans and co-workers [49–51] led to an expression for the "configurational temperature,"

$$\frac{1}{k_B T_{conf}} = -\frac{\left\langle \sum_{i=1}^{n} \nabla_i \cdot \mathbf{F}_i \right\rangle}{\left\langle \sum_{i=1}^{n} \mathbf{F}_i^2 \right\rangle}, \tag{11}$$

where $\mathbf{F}_i = -\nabla_i U^p$ is the total interaction force acting on particle i of an n-particle system. Therefore, the system temperature may be calculated equally well based on the atomistic positions only; i.e., T_{conf} is related solely to the system configuration comprising the particle positions without any regard to the particle momenta.

The configurational temperature calculated by Eq. (11) is generally known to be very accurate (i.e., close to the temperature calculated from Eq. (10) and also the traditional kinetic temperature based on the particle momenta) and statistically reliable (i.e., less affected by system-size effects). Thus it has been applied to a number of physical systems (e.g., chain molecules [51], charge-stabilized colloidal systems [52], polypeptides [53], gravitationally-driven inhomogeneous systems [54], flowing polymeric melts [55], etc.) under equilibrium or nonequilibrium conditions. The configurational temperature expression has been further extended for physical systems involving hard-core or discontinuous potentials [56]. Very recently, a comprehensive analysis of the fundamental aspects of the configurational temperature for nonequilibrium systems has been performed through extensive NEMD and NEMC simulations [57], suggesting that in order to define a physically meaningful configurational temperature for polymeric systems under nonequilibrium conditions, the dynamical effects created by the external fields should be excluded.

Although strictly valid only for equilibrium states, this idea can be extended to flowing systems by invoking the assumption of a local or quasi-thermodynamic equilibrium, which states that materials in steady nonequilibrium states follow equilibrium relationships within a local environment; this is standard protocol in the theory of nonequilibrium thermodynamics [1]. However, a more rigorous argument may be formulated in terms of a generalized ensemble. Following the procedure suggested by Ilg [58], the expression of the configurational temperature can be further generalized by applying a generalized canonical ensemble [57] such as the one adopted here—see Eqs. (1)–(3). The probability density function $\rho_{[\boldsymbol{\lambda}]}$ with the Lagrange multipliers $\boldsymbol{\lambda}$ is written as

$$\rho_{[\boldsymbol{\lambda}]}(\mathbf{z}) = \frac{1}{Q(\boldsymbol{\lambda})} \exp(-\beta H(\mathbf{z}) - \sum_k \lambda_k \Pi_k(\mathbf{z})), \tag{12}$$

$$Q(\boldsymbol{\lambda}) = \int \exp(-\beta H(\mathbf{z}) - \sum_k \lambda_k \Pi_k(\mathbf{z})) \quad d\mathbf{z}, \tag{13}$$

where $\mathbf{z}$ represents the full phase-space comprising both the position ($\mathbf{r}$) and momentum ($\mathbf{p}$) coordinates of all particles in the system. We then write the ensemble average of the sum of the square of the force acting on each particle, $\mathbf{F}_i = -\nabla_i U^p$ (the denominator of Eq. (11)) as

$$\begin{aligned} \left\langle \sum_{i=1}^{n} \mathbf{F}_i^2 \right\rangle &= \int d\mathbf{z}\, \rho_{[\boldsymbol{\lambda}]}(\mathbf{z}) \sum_{i=1}^{N} \mathbf{F}_i^2 \\ &= \frac{1}{Q(\boldsymbol{\lambda})} \int d\mathbf{z} (\sum_{i=1}^{n} \nabla_i U^p \cdot \nabla_i U^p) \exp(-\beta H(\mathbf{z}) - \sum_k \lambda_k \Pi_k(\mathbf{z})) \\ &= \frac{1}{Q(\boldsymbol{\lambda})} \int d\mathbf{z} \sum_{i=1}^{n} \nabla_i U^p \cdot \{-\beta^{-1}[\nabla_i \exp(-\beta H - \sum_k \lambda_k \Pi_k) + (\sum_k \lambda_k \nabla_i \Pi_k) \exp(-\beta H - \sum_k \lambda_k \Pi_k)]\} \\ &= \beta^{-1} \left\langle \sum_{i=1}^{n} \nabla_i^2 U^p \right\rangle - \beta^{-1} \left\langle \sum_{i=1}^{n} (\nabla_i U^p \cdot \sum_k \lambda_k \nabla_i \Pi_k) \right\rangle \end{aligned} . \tag{14}$$

Therefore, the configurational temperature can be defined as [57,58]

$$\frac{1}{k_B T_{\text{conf}}} = -\frac{\left\langle \sum_{i=1}^{n} \nabla_i \cdot \mathbf{F}_i \right\rangle - \left\langle \sum_{i=1}^{n} (\mathbf{F}_i \cdot \sum_k \lambda_k \nabla_i \Pi_k) \right\rangle}{\left\langle \sum_{i=1}^{n} \mathbf{F}_i^2 \right\rangle}. \tag{15}$$

In the present study where the Lagrange multiplier $\boldsymbol{\lambda}$ is equal to $-\boldsymbol{\alpha}$ and $\boldsymbol{\Pi}$ is equal to $\sum_{l=1}^{N_{ch}} \tilde{\mathbf{c}}_l$, it is found to be

$$\begin{aligned} \frac{1}{k_B T_{\text{conf}}} &= -\frac{\left\langle \sum_{i=1}^{n} \nabla_i \cdot \mathbf{F}_i \right\rangle + \boldsymbol{\alpha} : \left\langle \sum_{i=1}^{n} (\mathbf{F}_i \cdot (\nabla_i \sum_{l=1}^{N_{ch}} \tilde{\mathbf{c}}_l)) \right\rangle}{\left\langle \sum_{i=1}^{n} \mathbf{F}_i^2 \right\rangle} \\ &= -\frac{\left\langle \sum_{i=1}^{n} \nabla_i \cdot \mathbf{F} \right\rangle + \boldsymbol{\alpha} : \sum_{l=1}^{N_{ch}} \frac{6(\mathbf{F}_{l,N_l} - \mathbf{F}_{l,1})\mathbf{R}_l}{\left\langle R^2(N_l) \right\rangle_{eq}}}{\left\langle \sum_{i=1}^{n} \mathbf{F}_i^2 \right\rangle} \end{aligned} , \tag{16}$$

where $\mathbf{R}_l$ is the end-to-end vector of the lth-chain and $\left\langle R^2(N_l) \right\rangle_{eq}$ denotes the mean-square chain end-to-end distance of length N_l-mers at equilibrium. $\mathbf{F}_{l,1}$ and $\mathbf{F}_{l,N_l}$ are the forces acting on the first atom and the last atom, respectively, of the lth-chain. Considering that the force acting on an atom is statistically random and furthermore only the two end atoms are involved, the field term in Eq. (16) in the numerator is generally assumed to make a negligible contribution.

Using T_{conf}, structural changes of the system in response to external flow fields can be related to the theoretical temperature that the molecules effectively experience with regard to chain configurations and ordering, even though the actual temperature of the system has not changed. Essentially, this temperature under flow represents the effective temperature that the liquids would experience based on their altered configurations, were they under quiescent conditions.

Fig. 8 displays data for ΔT_{conf} vs. tr($\tilde{\mathbf{c}}$) for each system (inset, ΔT_{conf} vs. α_{xx}) (the main graph was also presented in Ref. [28]). The main graph can be obtained using the inset to determine ΔT_{conf} as a function of α_{xx}, and then calculating tr($\tilde{\mathbf{c}}$) for each value of α_{xx}. The data reveal a monotonic decrease of T_{conf} at all values of temperature, indicating that the flow field causes the molecules to become more oriented, stretched, and packed into structures that they would quiescently assume at lower actual temperatures. All four of the lines in Fig. 8 intersect at essentially the same point, corresponding to a value of tr($\tilde{\mathbf{c}}$) of about 14 and a ΔT_{conf} of about −4 °C.

This provides further evidence of a flow-induced crystalline phase at the lower two temperatures once past the critical field strengths. These results are consistent with experiments [2,3,16], which revealed that the stresses induced under flow effectively raise the crystallization temperature of the liquid state, offering a physical explanation for the long-standing experimental and theoretical issue of the flow-induced melting point elevation. Remarkably, the experimentally reported 15–20 °C increase of T_{m} for a polyethylene crystal [16] compares very well with the simulated value of ∼13 °C decrease of T_{conf} at $T = 350$ K and $\alpha_{xx} = 1.0$.

This linear behavior of temperature change with tr($\tilde{\mathbf{c}}$) was first noticed by Ionescu et al. [59,60] in an experimental study of high-density polyethylene (HDPE), where data taken at three different temperatures revealed linear behavior that superimposed, as above, to reveal a common value of the slope. This remarkable result was rationalized based upon a simple expression for the extended internal energy to include conformational effects,

$$U(S, V, \tilde{\mathbf{c}}) = U_{eq}(S, V) + EU_{eq}(S, V)[\text{tr}(\tilde{\mathbf{c}}) - 3], \tag{17}$$

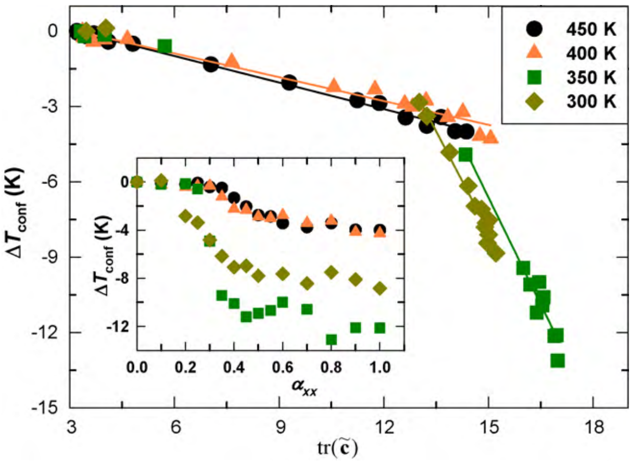

Fig. 8. Configurational temperature change, $\Delta T_{conf} (= T_{conf,noneq} - T_{conf,eq})$ vs. tr($\tilde{\mathbf{c}}$). The inset graphs ΔT_{conf} vs. α_{xx}. The lines represent the best linear fits to the simulation data for each system.

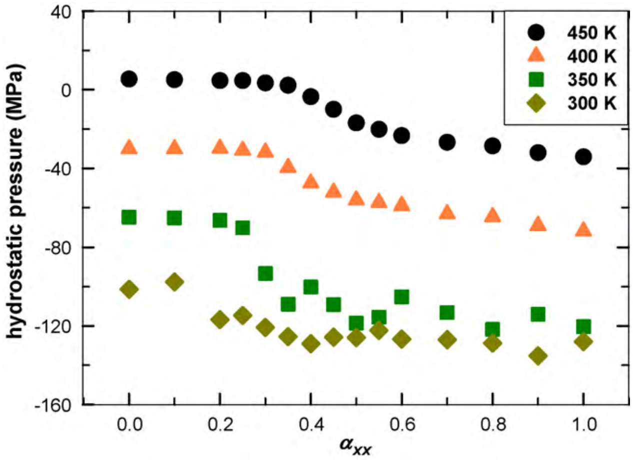

Fig. 9. Hydrostatic pressure with respect to the flow field for each temperature.

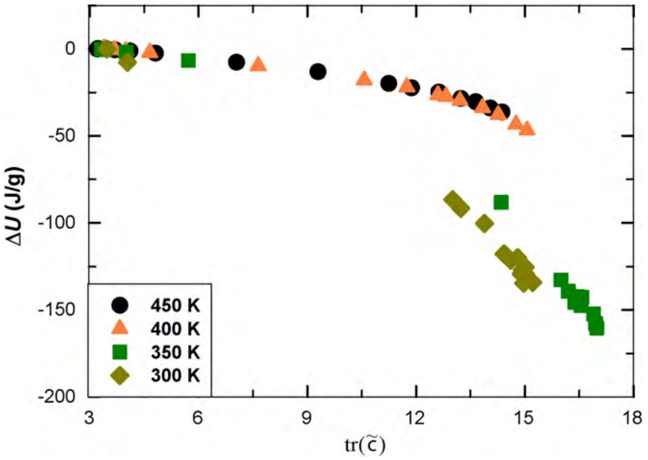

Fig. 10. Plot of the internal energy change ΔU vs. $\mathrm{tr}(\tilde{\mathbf{c}})$. The standard errors are commensurate with the size of the symbols.

where $U_{eq}(S,V)$ is the equilibrium internal energy, independent of molecular configuration, and E is a constant that describes the strength of the conformational effect on the internal energy. A "nonequilibrium temperature," T_{NE}, was then derived by taking the partial derivative of Eq. (17) with respect to entropy [59,60],

$$T_{NE} = T_{eq} + ET_{eq}[\mathrm{tr}(\tilde{\mathbf{c}}) - 3], \tag{18}$$

where $T_{eq} = \partial U_{eq}/\partial S$ is the standard thermodynamic temperature at equilibrium. The parameter E then is independent of the equilibrium temperature and equivalent to the slopes mentioned above. The parameter E is found to be approximately equal to $(-7.8 \pm 0.2) \times 10^{-4}$ for $T = 450$ K and $(-7.9 \pm 0.4) \times 10^{-4}$ for $T = 400$ K for the melt phase, and $(-8.1 \pm 0.6) \times 10^{-3}$ for $T = 350$ K and $(-8.8 \pm 0.4) \times 10^{-3}$ for $T = 300$ K for the crystalline phase.

Another interesting feature of Fig. 8 is that it provides a semi-quantitative prediction of the critical value of flow strength necessary for the crystallization event as a function of temperature. This critical value of α_{xx} can be estimated using the value of $\mathrm{tr}(\tilde{\mathbf{c}})$ where the two pairs of lines in Fig. 8 intersect, since these lines are essentially independent of temperature. This value of $\mathrm{tr}(\tilde{\mathbf{c}})$ is associated with a decrease in the value of T_{conf} of approximately 4 K. Hence a minimum change in T_{conf} of about 4–5 K seems to be necessary to observe a crystallization event, if it occurs at all, and this can then be associated with a particular value of α_{xx} using the inset graph of Fig. 8.

The experimental value of T_{m} under quiescent conditions for $C_{78}H_{158}$ is approximately 380 K [61] at $P = 1$ atm. Therefore, the two liquids with lower temperature values seem to be already below the experimental melting point. However, we should note that the density ($\rho = 0.7638$ g/cm^3) of the present system for all temperatures is quite smaller than the experimental density (approximately estimated as $\rho = 0.8$ g/cm^3) at $T = 380$ K and $P = 1$ atm for the corresponding PE melt [62]. Therefore, for the lower temperature systems ($T = 300$ and 350 K), the corresponding density at $P = 1$ atm will be even significantly larger (e.g., according to Table 1 in Ref. [62], $\rho = 0.956$ g/cm^3 at $T = 295$ K for $C_{78}H_{158}$ PE melt). Besides, there may be some uncertainties of the melting temperature predicted by the SKS model for a specific polyethylene liquid, since the model was not developed using T_{m} as a criterion. The problem lies in the severe computational requirements necessary to determine T_{m} with an acceptable degree of accuracy, given the presumed small changes in the depth of the energy wells near the melting point. According to the discussion of the previous paragraph, a realistic crystallization event could be simulated at a value of set point temperature that is 4 K above (definitely in the liquid regime) the experimental value of $T_{\mathrm{m}} \sim 380$ K and at $P = 1$ atm or $\rho = 0.8$ g/cm^3, with the critical value of α_{xx} determined using the inset graph of Fig. 8.

For more quantitative information regarding the density, we present in Fig. 9 the change of the hydrostatic pressure (calculated based on the virial theorem; see Section 2.4 in Ref. [63]) with respect to the field strength. (The kinetic and bond-stretching contributions as well as the long-range correction [63] were incorporated in the calculation.) As evident from the figure, the hydrostatic pressure decreases as the field strength increases for all temperatures, indicative of the increase of favorable (attractive) interactions between molecules under flow; this is physically reasonable since as the field increases the molecules become more stretched and aligned with each other. We further note that overall the pressure of the system appears to be smaller at lower temperatures over the whole range of α_{xx}. These results indicate that if we perform constant-pressure simulations at $P = 1$ atm instead of the present constant-volume simulations, the density of the system for each temperature will increase as the field increases (as possibly suggested by Fig. 7b). Furthermore, it is expected from the figure that the lower temperature systems will show even larger densities, which would further enhance the flow-induced crystallization and thus lead to a better crystalline structure of the FIC. Future work will address this issue.

Fig. 10 displays data for the total internal energy change vs. $\mathrm{tr}(\tilde{\mathbf{c}})$ at all four values of temperature. Similarly to Fig. 8, two sets of curves are evident, one corresponding to the two higher temperature liquids for all values of α_{xx} and the two lower temperature liquids below the critical values of α_{xx}, and another one corresponding to the lower temperature liquids above the critical α_{xx}. Again the data in the liquid phase appear to be essentially superimposed, and there is only a minor offset in the curves for the FIC phase. This suggests that a universally valid expression for a nonequilibrium heat capacity might be defined using T_{conf} as an appropriate thermodynamic variable.

Fig. 11 displays a plot of ΔU vs. ΔT_{conf} for the liquids at the four different set point temperatures. It is apparent that there exist two distinct regimes, one associated with the melt phase of the liquids at all four temperature values and the other with the crystalline phase occurring at the lower temperatures above the critical values of α_{xx}. Within statistical uncertainty, the slopes of all lines are approximately 9 J/(g K), irrespective of melt or FIC phase. In addition, by fitting only the data near the equilibrium states (i.e., at weak flow fields) of the melt phase at all four temperatures, the slope plus the kinetic contribution [≈0.89 J/(g K)] is found to be 2.75 ± 0.99 J/(g K) at $T = 450$ K and 2.23 ± 1.5 J/(g K)

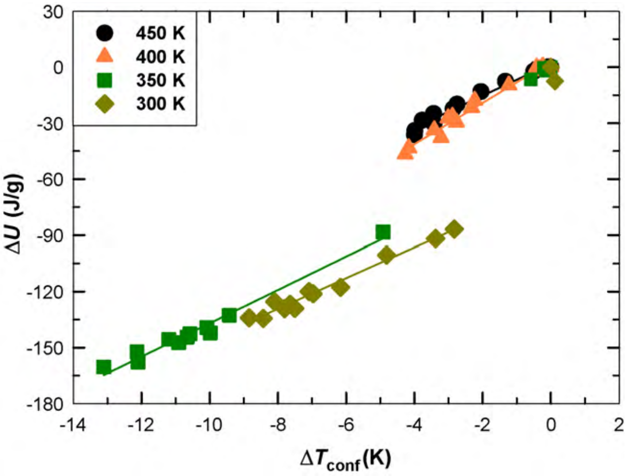

Fig. 11. Internal energy change ΔU vs. ΔT_{conf}. The lines represent the best linear fits to the simulation data for each system.

at $T = 400$ K (not enough data points lie within this α_{xx} range at the lower two temperature values for a meaningful calculation), which is close to the experimental heat capacity of amorphous polyethylene of 2.67 J/(g K) at $T = 450$ K and 2.52 J/(g K) at $T = 400$ K [44]. This result might be expected by applying the most fundamental postulate underlying the fluctuation-dissipation theorem within linear irreversible thermodynamics, which stipulates that the dynamical mechanisms occurring strictly at equilibrium are assumed to be exactly the same as those occurring under nonequilibrium conditions as long as the external field applied to the system is sufficiently small compared to thermal Brownian forces. In this connection, under very weak external flow strengths, the nonequilibrium heat capacity represented by the ratio between the change of the system energy and the change of the configurational temperature (both of which are directly associated with the change of the overall, large-scale system structure due to the external field) may be quantitatively similar to the equilibrium heat capacity represented by the conventional definition of the ratio between the system energy change and the system temperature at equilibrium states. The present result appears to confirm this fundamental physical aspect. Incidentally, the structural changes induced by applying weak external fields could be equally induced by changing the system temperature under equilibrium conditions. However, for significant values of field strength, the slopes mentioned above might correspond to a nonequilibrium value of heat capacity, as defined via a quasi-equilibrium extension of the equilibrium definition of the heat capacity,

$$C_V^{NE} \equiv \left. \frac{\partial U_{NE}}{\partial T_{conf}} \right|_{V,\tilde{\mathbf{c}}} \tag{14}$$

which accounts for conformation changes in the macromolecular configurational state of the chain liquids. This nonequilibrium definition of a thermodynamic quantity, in this case the heat capacity, with a similar form to the equilibrium heat capacity, would have far reaching implications with regard to nonequilibrium statistical mechanics, were it to prove universally valid.

4. Conclusions

Simulations were performed of the development of a flow-induced crystalline (FIC) phase occurring in an isotropic polymeric liquid when subjected to a strong uniaxial elongational flow using a thermodynamically well-founded nonequilibrium Monte Carlo methodology. The FIC structure was found to have a similar global long-range order to the real crystals. The sharp Bragg peaks observed at small k-values (i.e., <1.5 Å^{-1}) and the long-range local density correlation in the FIC phase demonstrated the primary characteristics of real crystallites. Meanwhile, the Bragg peaks within the range of $k = 2$–4 Å^{-1} existing in the n-eicosane real crystal were weakly reproduced in the FIC, indicating a lack of certain crystalline planes in the simulated FIC. These most likely were due to a relatively low degree of lateral packing, which might be due to the fact that the simulations were performed at constant volume, rather than constant pressure. The abrupt, discontinuous phase transition in the overall conformational behavior of the crystalline state further illustrated that even short-chain systems can undergo a coil-stretch transition and create an extended-chain crystal (shish) under strong flow fields; this seems to corroborate a recent experimental finding [19] that the shish contains all chain lengths. Furthermore, a rudimentary hexagonal array of chains was observed in the FIC created at $T = 300$ and 350 K, but no such regular array structure was found in the highly oriented melts at $T = 400$ and 450 K even at high field strengths ($\alpha_{xx} = 1.0$). Furthermore, the analysis of the simulation data by use of the configurational temperature offered a physically plausible microscopic origin for the long-standing issue of the melting point elevation under flow, and a plausible extension of equilibrium properties to nonequilibrium conditions.

Acknowledgements

This work was supported by the National Science Foundation under Grant No. CBET-0742679 and used the resources of the PolyHub Engineering Virtual Organization.

References

[1] A.N. Beris, B.J. Edwards, Thermodynamics of Flowing Systems with Internal Microstructure, Oxford University Press, New York, 1994.
[2] C. Rangel-Nafaile, A.B. Metzner, K.F. Wissbrun, Analysis of stress-induced phase separations in polymer solutions, Macromolecules 17 (1984) 1187–1195.
[3] F.L. Binsbergen, Orientation-induced nucleation in polymer crystallization, Nature 211 (1966) 516–517.
[4] A. Keller, M.J. Machin, Oriented crystallization in polymers, J. Macromol. Sci. (Phys.) B1 (1967) 41–91.
[5] A.J. McHugh, E.H. Forrest, A discussion of nucleation and growth in flow-induced crystallization from solution and an improved model for the growth process, J. Macromol. Sci. (Phys.) B11 (1975) 219–238.
[6] M.R. Mackley, A. Keller, Flow induced crystallization of polyethylene melts, Polymer 14 (1973) 16–20.
[7] C.L. Sieglaff, K.J. O'Leary, Melt transitions of polypropylene, Trans. Soc. Rheol. 14 (1970) 49–64.
[8] A.C. Bushman, A.J. McHugh, A continuum model for the dynamics of flow-induced crystallization, J. Polym. Sci.: B Polym. Phys. 34 (1996) 2393–2407.
[9] A.K. Doufas, I.S. Dairenieh, A.J. McHugh, A continuum model for flow-induced crystallization of polymer melts, J. Rheol. 43 (1999) 85–109.
[10] H. Zuidema, G.W.M. Peters, H.E.H. Meijer, Development and validation of a recoverable strain-based model for flow-induced crystallization of polymers, Macromol. Theory Simul. 10 (2001) 447–460.
[11] A.K. Doufas, A.J. McHugh, C. Miller, Simulation of melt spinning including flow-induced crystallization: part I. Model development and predictions, J. Non-Newtonian Fluid Mech. 92 (2000) 27–66.
[12] S. Coppola, N. Grizzuti, P.L. Maffettone, Microrheological modeling flow-induced crystallization, Macromolecules 34 (2001) 5030–5036.
[13] S. Coppola, L. Balzano, E. Gioffredi, P.L. Maffettone, N. Grizzuti, Effects of the degree of undercooling on flow induced crystallization in polymer melts, Polymer 45 (2004) 3249–3256.
[14] J. Mukherjee, S. Wilson, A.N. Beris, Flow-induced nonequilibrium thermodynamics of lamellar semicrystalline polymers, J. Non-Newtonian Fluid Mech. 120 (2004) 225–240.
[15] J.M. Schultz, Polymer Crystallization: The Development of Crystalline Order in Thermoplastic Polymers, Oxford University Press, New York, 2001.
[16] R.H. Somani, L. Yang, L. Zhu, B.S. Hsiao, Flow-induced shish-kebab precursor structures in entangled polymer melts, Polymer 46 (2005) 8587–8623.
[17] H. Janeschitz-Kriegl, E. Ratajski, M. Stadlbauer, Flow as an effective promotor of nucleation in polymer melts: a quantitative evaluation, Rheol. Acta 42 (2003) 355–364.
[18] B.S. Hsiao, L. Yang, R.H. Somani, C.A. Avila-Orta, L. Zhu, Unexpected shish-kebab structure in a sheared polyethylene melt, Phys. Rev. Lett. 94 (2005) 117802.

[19] S. Kimata, et al., Molecular basis of the shish-kebab morphology in polymer crystallization, Science 316 (2007) 1014–1017.

[20] G. Reiter, G.R. Strobl (Eds.), Progress in Understanding Polymer Crystallization, Springer, Berlin, 2007.

[21] M.S. Lavine, N. Waheed, G.C. Rutledge, Molecular dynamics simulation of orientation and crystallization of polyethylene during uniaxial extension, Polymer 44 (2003) 1771–1779.

[22] M.J. Ko, N. Waheed, M.S. Lavine, G.C. Rutledge, Characterization of polyethylene crystallization from an oriented melt by molecular dynamics simulation, J. Chem. Phys. 121 (2004) 2823–2832.

[23] I. Dukovski, M. Muthukumar, Langevin dynamics simulations of early stage shish-kebab crystallization of polymers in extensional flow, J. Chem. Phys. 118 (2003) 6648–6655.

[24] W. Hu, D. Frenkel, V.B.F. Mathot, Simulation of shish-kebab crystallite induced by a single prealigned macromolecule, Macromolecules 35 (2002) 7172–7174.

[25] R.S. Graham, P.D. Olmsted, Coarse-grained simulations of flow-induced nucleation in semicrystalline polymers, Phys. Rev. Lett. 103 (2009) 115702.

[26] C. Baig, B.J. Edwards, D.J. Keffer, H.D. Cochran, A proper approach for nonequilibrium molecular dynamics simulations of planar elongational flow, J. Chem. Phys. 122 (2005) 114103.

[27] T.C. Ionescu, C. Baig, B.J. Edwards, D.J. Keffer, A. Habenschuss, Structure formation under steady-state isothermal planar elongational flow of n-eicosane: a comparison between simulation and experiment, Phys. Rev. Lett. 96 (2006) 037802.

[28] C. Baig, B.J. Edwards, Atomistic simulation of flow-induced crystallization at constant temperature, Europhys. Lett. 89 (2010) 36003.

[29] V.G. Mavrantzas, H.C. Öttinger, Atomistic Monte Carlo simulations of polymer melt elasticity: their nonequilibrium thermodynamics GENERIC formulation in a generalized canonical ensemble, Macromolecules 35 (2002) 960–975.

[30] C. Baig, V.G. Mavrantzas, Thermodynamically guided nonequilibrium Monte Carlo method for generating realistic shear flows in polymeric systems, Phys. Rev. Lett. 99 (2007) 257801.

[31] C. Baig, V.G. Mavrantzas, Multiscale simulation of polymer melt viscoelasticity: expanded-ensemble Monte Carlo coupled with atomistic nonequilibrium molecular dynamics, Phys. Rev. B 79 (2009) 144302.

[32] B.J. Edwards, A.N. Beris, Noncanonical Poisson bracket for nonlinear elasticity with extension to viscoelasticity, J. Phys. A: Math. Gen. 24 (1991) 2461–2480.

[33] B.J. Edwards, A.N. Beris, Unified view of transport phenomena based on the generalized bracket formulation, Ind. Eng. Chem. Res. 30 (1991) 873–881.

[34] P.V.K. Pant, D.N. Theodorou, Variable connectivity method for the atomistic Monte Carlo simulation of polydisperse polymer melts, Macromolecules 28 (1995) 7224–7234.

[35] K. Daoulas, A.F. Terzis, V.G. Mavrantzas, Variable connectivity methods for the atomistic Monte Carlo simulation of inhomogeneous and/or anisotropic polymer systems of precisely defined chain length distribution: tuning the spectrum of chain relative chemical potentials, Macromolecules 36 (2003) 6674–6682.

[36] C. Baig, O. Alexiadis, V.G. Mavrantzas, Advanced Monte Carlo algorithm for the atomistic simulation of short- and long-chain branched polymers: implementation for model H-shaped, A3AA3 multiarm (Pom-Pom), and short-chain branched polyethylene melts, Macromolecules 43 (2010) 986–1002.

[37] J.M Kim, D.J. Keffer, M. Kröger, B.J. Edwards, Rheological and entanglement characteristics of linear chain polyethylene liquids in planar Couette and planar elongational flows, J. Non-Newtonian Fluid Mech. 152 (2008) 168–183.

[38] J.M. Kim, B.J. Edwards, D.J. Keffer, B. Khomami, Dynamics of individual molecules of linear polyethylene liquids under shear: atomistic simulation and comparison with a free-draining bead-rod chain, J. Rheol. 54 (2010) 283–310.

[39] C. Baig, B.J. Edwards, D.J. Keffer, H.D. Cochran, V.A. Harmandaris, Rheological and structural studies of linear polyethylene melts under planar elongational flow using nonequilibrium molecular dynamics simulations, J. Chem. Phys. 124 (2006) 084902.

[40] A.M. Kraynik, D.A. Reinelt, Int. J. Multiphase Flow 18 (1992) 1045–1059.

[41] J.I. Siepmann, S. Karaboni, S.B. Smit, Simulating the critical behaviour of complex fluids, Nature 365 (1993) 330–332.

[42] C. Baig, B.J. Edwards, D.J. Keffer, H.D. Cochran, Rheological and structural studies of liquid decane, hexadecane, and tetracosane under planar elongational flow using nonequilibrium molecular-dynamics simulations, J. Chem. Phys. 122 (2005) 184906.

[43] P.G. de Gennes, Coil-stretch transition of dilute flexible polymers under ultrahigh velocity gradients, J. Chem. Phys. 60 (1974) 5030–5042.

[44] U. Gaur, B. Wunderlich, Heat capacity and other thermodynamic properties of linear macromolecules: II Polyethylene, J. Phys. Chem. Ref. Data 10 (1981) 119–152.

[45] J.E. Spruiell, Personal communication, 2009.

[46] L.T. Eremenko, Principles of the change in density in homologous series of liquid and crystalline hydrocarbons, Russ. Chem. Bull. 17 (1968) 1012–1016.

[47] H.H. Rugh, Dynamical approach to temperature, Phys. Rev. Lett. 78 (1997) 772–774.

[48] H.H. Rugh, A geometric, dynamical approach to thermodynamics, J. Phys. A: Math. Gen. 31 (1998) 7761–7770.

[49] G. Ayton, O.G. Jepps, D.J. Evans, On the validity of Fourier's law in systems with spatially varying strain rates, Mol. Phys. 96 (1999) 915–920.

[50] O.G. Jepps, G. Ayton, D.J. Evans, Microscopic expressions for the thermodynamic temperature, Phys. Rev. E 62 (2000) 4757–4763.

[51] L. Lue, O.G. Jepps, J. Delhommelle, D.J. Evans, Configurational thermostats for molecular systems, Mol. Phys. 100 (2002) 2387–2395.

[52] Y. Han, D.G. Grier, Configurational temperature of charge-stabilized colloidal monolayers, Phys. Rev. Lett. 92 (2004) 148301.

[53] P. Pliego-Pastrana, M.D. Carbajal-Tinoco, Polypeptide foldings obtained with effective pair potentials, J. Chem. Phys. 122 (2005) 244908.

[54] R.S. Saksena, L.V. Woodcock, Density functional approach to thermodynamics of self-assembly, J. Chem. Phys. 122 (2005) 164501.

[55] J. Delhommelle, D.J. Evans, Comparison of thermostatting mechanisms in NVT and NPT simulations of decane under shear, J. Chem. Phys. 115 (2001) 43–49.

[56] G. Rickayzen, D.M. Heyes, A configurational temperature for molecules with hard-core or discontinuous interactions, J. Chem. Phys. 127 (2007) 144512.

[57] C. Baig, B.J. Edwards, Analysis of the configurational temperature of polymeric liquids under shear and elongational flows using nonequilibrium molecular dynamics and Monte Carlo simulations, J. Chem. Phys., doi:10.1063/1.3415085, in press.

[58] P. Ilg, Personal communication, 2009.

[59] T.C. Ionescu, B.J. Edwards, D.J. Keffer, V.G. Mavrantzas, Energetic and entropic elasticity of nonisothermal flowing polymers: experiment, theory, and simulation, J. Rheol. 52 (2008) 105–140.

[60] T.C. Ionescu, V.G. Mavrantzas, D.J. Keffer, B.J. Edwards, Atomistic simulation of energetic and entropic elasticity in short-chain polyethylenes, J. Rheol. 52 (2008) 567–589.

[61] J. Pak, B. Wunderlich, Melting and crystallization of polyethylene of different molar mass by calorimetry, Macromolecules 34 (2001) 4492–4503.

[62] G.T. Dee, T. Ougizawa, D.J. Walsh, The pressure–volume–temperature properties of polyethylene, poly(dimethyl siloxane), poly(ethylene glycol) and poly(propylene glycol) as a function of molecular weight, Polymer 33 (1992) 3462–3469.

[63] M.P Allen, D.J. Tildesley, Computer Simulation of Liquids, Oxford University Press, New York, 1987.